Solvent-Free Synthesis of Cu$_2$ZnSnS$_4$ Nanocrystals: A Facile, Green, Up-scalable Route for Low Cost Photovoltaic Cells†

Bo-In Park,‡[ab] Yoonjung Hwang,‡[cd] Seung Yong Lee,[a] Jae-Seung Lee,[b] Jong-Ku Park,[a] Jeunghyun Jeong,[c] Jin Young Kim,[c] BongSoo Kim,[c] So-Hye Cho[*a] and Doh-Kwon Lee[*cd]

Table of content entry
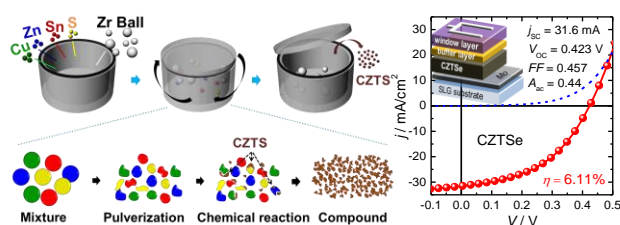
Cu$_2$ZnSnS$_4$ nanocrystals were synthesized by a solvent-free mechanochemical process and successfully applied to fabricate Cu$_2$ZnSnSe$_4$ solar cells, resulting in power conversion efficiencies over 6%.

Abstract

Efficient $Cu_2ZnSnSe_4$ (CZTSe) solar cells were fabricated with a simple, environmentally friendly, and scalable synthetic method for Cu_2ZnSnS_4 (CZTS) nanocrystals. CZTS nanoparticles were mechanochemically synthesized from elemental precursors on a relatively large scale (~20 g), during which no solvents or additives were used, thus alleviating the complex process of particle synthesis. An analysis of the time evolution of the crystalline phase and morphology of precursor powders revealed that the formation of the CZTS compound was completed in 0.5 h once initiated, suggesting that the mechanochemically-induced self-propagating reaction prevails. CZTS ink was prepared by dispersing the as-synthesized nanoparticles in an environmentally benign solvent (160 mg/mL in ethanol) without using any additives, after which it was cast onto Mo-coated glass substrates by a doctor-blade method. Subsequent reactive annealing at 560 ℃ under a Se-containing atmosphere resulted in substantial grain growth along with the nearly complete substitution of Se. The CZTSe solar cells therefrom exhibited power conversion efficiency levels as high as 6.1% (based on the active area, 0.44 cm^2) with a relatively high open-circuit voltage (0.42 V) in comparison with the bandgap energy of 1.0 eV.

Introduction

Since the discovery of the photovoltaic effect in the Cu_2ZnSnS_4 (CZTS) quaternary compound in 1988,[1] $Cu_2ZnSn(S_{1-x}Se_x)_4$ (CZTSSe) has been studied intensively as an inexpensive and earth-abundant alternative to $Cu(In_{1-x}Ga_x)(S_{1-y}Se_y)_2$ (CIGSSe).[2] While CZTSSe is an earth-abundant material, it also has a high degree of similarity with CIGSSe in terms of its opto-electronic properties, such as a high absorption coefficient ~10^4 cm^{-1} and near-optimum bandgap energy (E_g) of 1.0 to 1.5 eV. Both characteristics have drawn a great deal of attention to CZTSSe.[3,4] Thus, various techniques that have been developed for the

fabrication of CIGSSe thin films have been applied to realize high-quality CZTS thin films. To take full advantage of the low cost of CZTS materials, the processing cost also has to be taken into account. In this respect, non-vacuum processes such as electrochemical deposition and solution deposition are much more preferred than vacuum processes. Among the achievements thus far, Teodor *et al.* have demonstrated the highest efficiency of 12.6% using a hydrazine-mediated solution deposition method for CZTSSe absorber layers.[5] This represents a remarkable advance considering that the highest efficiency of a CIGSSe cell by a non-vacuum process has remained around 15% to date.[6] Moreover, vacuum processes, often considered as highly equipped methods, only offer a maximum efficiency level of 9.15% for CZTSe solar cells.[7] Unfortunately, however, the hydrazine method is associated with safety issues due to the highly toxic and potentially explosive nature of hydrazine.

To address this issue, other non-vacuum approaches involving the use of nanocrystal inks have been developed.[8–13] With these methods, binary to quaternary nanocrystals were synthesized typically via chemical reactions in organic solvents such as oleylamine, octadecene, trioctylphosphine and dodecanethiol, which are comparatively expensive, environmentally less benign and also can leave carbon residue in the absorber layer. Hence, the use of non-toxic and low-cost solvents for CZTS inks has been suggested.[14–16] Woo *et al.* used an ethanol-based CZTS ink for a bandgap-graded CZTSSe solar cell and demonstrated an efficiency of 7.1 %.[14] The CZTS ink was prepared by the wet-milling processing of particulate precursors (Cu_2S, Zn, Sn, and S) in ethanol. This approach offers a simple and inexpensive alternative for the fabrication of CZTSSe solar cells and does not leave carbon impurities after annealing, as no high-boiling-point organic additives are present. However, their ink materials contain unreacted species and other intermediate compounds which are unstable due to the surface activation caused by attrition during the milling process. On the other hand, the dry mechanochemical synthesis of CZTS powders has been reported by

several research groups.[17,18] During this type of synthesis, milling leads to attrition, mixing and contact reactions among the elemental precursors of Cu, Zn, Sn, and S, inducing physical and/or chemical changes of the reactants and intermediates. This method has several advantages over solution synthesis, such as high level of productivity, a short processing time, and no need for additives (or solvents). In 2011, Wang and Gong were the first to demonstrate that CZTS compounds could be directly formed from its elemental precursors after planetary ball milling for 25 h.[17] In 2012, Gao *et al*. showed that the milling of the elemental precursors for a rather short period of 20 min with a subsequent heat treatment at 550 $^\circ$C for 5 h can provide CZTS powders with high phase purity.[18] Unfortunately, however, it was not proved in both cases that CZTS compounds prepared in such a manner can efficiently serve as an absorption layer for photovoltaic (PV) devices.

Herein, we demonstrate the solvent-free mechanochemical synthesis of CZTS nanoparticles as a highly cost-effective and environmentally benign route for fabricating a light-absorbing layer for photovoltaic cells. CZTS nanocrystals were synthesized with high crystallinity on a scale of tens of grams from readily available elemental powder precursors. No organic solvents or additives were used during the synthetic process, thus circumventing the formation of by-products. The dry synthetic process also alleviates the subsequent steps, such as washing, centrifuging, drying, and pyrolysis. Moreover, the resulting product in a dry powder form offers high stability under ambient conditions along with easy handling. The time evolution of the crystalline phase and morphology during the mechanochemical process was analyzed, leading to the suggestion of the reaction pathway to the CZTS compound. Thin films were formed by preparing a binder-free ink in ethanol and using a doctor-blade method to keep the processing cost as low as possible and avoid carbon contamination in the absorber layer.[19] By reactive annealing under selenium vapor, the CZTS nanoparticulate film was converted into low-bandgap $Cu_2ZnSnSe_4$ (CZTSe with E_g = 1.0 eV), which is regarded as

one of the most promising candidates for the bottom cell of a low-cost tandem structure. Furthermore, the volume expansion associated with selenization can be utilized during the densification of thin films. The resulting CZTSe thin film exhibited a power conversion efficiency (PCE) of 6.1% in the conventional configuration of a CZTS solar cell.

RESULTS AND DISCUSSION

Structural analysis of CZTS powders

Fig. 1(a,b) shows X-ray diffraction (XRD) patterns of milled powders intermittently picked up while milling up to 5 h using zirconia balls at 500 rpm. One can recognize that abrupt and significant changes occurred at 3 h in the constituent phases of the milled powders. The XRD pattern for the sample milled for 3 h exhibited diffraction peaks that can be assigned to the CZTS phase (JCPDS card no. 26-0575). Due to the similarity of the XRD patterns for CZTS and other binary and ternary sulfides, the Raman spectrum (using a 514.5 nm Ar-ion laser) for the powder milled for 5 h was analyzed to examine the phase purity of the as-synthesized nanoparticles, as shown in Fig. 1(c). Despite the ambiguity associated with peak deconvolution, the characteristic Raman scatterings at 289, 335, and 364 cm^{-1} can be assigned to kesterite CZTS.[20,21] Impurity phases such as Cu_2S (at around 475 cm^{-1}),[21] SnS_2 (315 cm^{-1}),[22] Cu-Sn-S compounds (303, 318 cm^{-1}),[23] and ZnS (350 cm^{-1})[21] were not detected, which could be partly due to the low sensitivity of the 514.5 nm-excitation for those phases or the peak broadening associated with the nanoparticulate nature of the synthesized powder. It is noted, however, that as the mechanochemical reaction was driven in a closed system (in a sealed vessel), local Sn loss, which may cause phase separation, could be minimized during the synthetic process, if not completely ruled out. Fig. 1(b) shows the XRD patterns of the milled powders, as obtained in an attempt to understand the detailed phase evolution between 2 h and 3 h, revealing that the dramatic phase change took place between 2 h 20 min and 2 h

30 min. The (112) plane of kesterite CZTS first appears in 2 h 30 min, and its intensity at 3 h

increases by no more than 5% upon further milling for an extended time of up to 5 h. This

indicates that most of the phase transformation was, once initiated, accomplished within half

an hour.
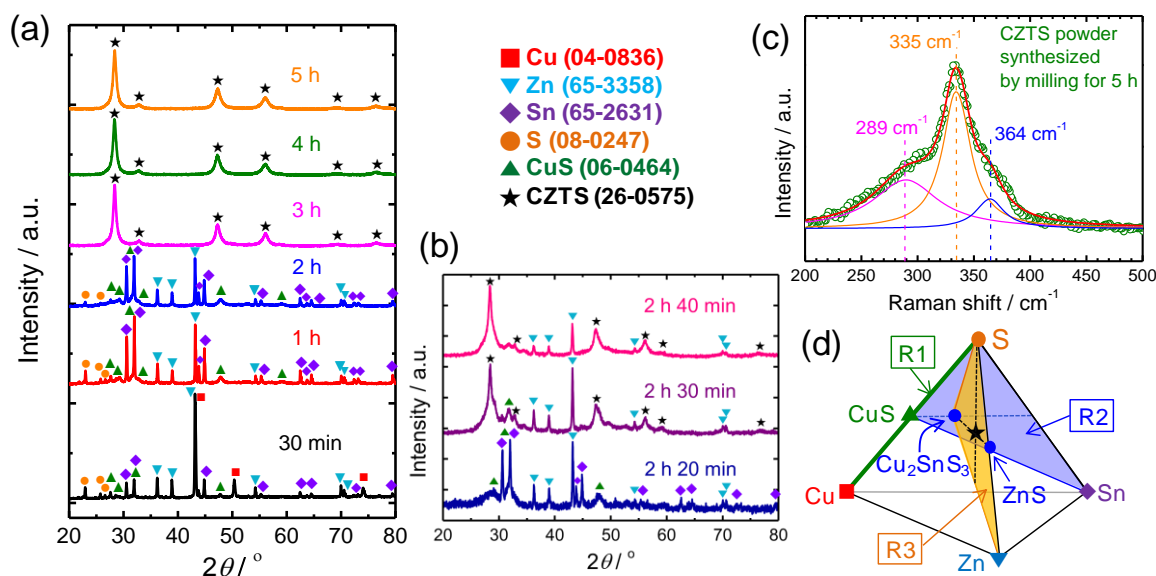
Fig. 1. Phase evolution of Cu, Zn, Sn, and S powder mixture to CZTS: X-ray diffraction patterns for the precursors milled at 500 rpm (a) for 30 min, 1 h, 2 h, 3 h, 4 h and 5 h, (b) for 2 h 20 min, 2 h 30 min, and 2 h 40 min, (c) Raman spectrum (using 514.5 nm excitation) of CZTS powder synthesized by ball-milling for 5 h, and (d) a schematic of quaternary phase diagram and reaction pathway. Note that the numerals in the parentheses of the legend stand for the JCPDS card numbers.

A closer examination of the XRD patterns allows us to suggest a reaction pathway to

CZTS: the CuS peaks (the most intense peak at 32.0°) already exist at 30 min, while the Cu

peaks (at 50.4°) disappear in 1 h, indicating the formation of CuS at the initial stage of the

reaction (as represented by line R1 in the schematic of the quaternary phase diagram shown

in Fig. 1(d)). Cu-Sn or Cu-Zn alloys (*e.g.*, Cu_6Sn_5 or Cu_5Zn_8)[24,25] were not detected at any

stage. A noticeable decrease in the amount of Sn (at 30.6°) was first recognized at 2 h 30 min as shown in Fig. 1(b). At the same time, a strong (112) reflection CZTS at 28.4° along with its shoulder peaks at 29.1° developed, while a considerable amount of elemental Zn (at 43.2°) remained unreacted. This implies that the products at 2 h 30 min include at least a Zn-deficient compound (*e.g.*, Cu-Sn-S phases) formed through the consumption of CuS and elemental Sn (R2 in Fig. 1(d)). Here, we do not exclude the formation of ZnS, as its XRD pattern is practically indistinguishable from that of kesterite CZTS,[25] particularly in the nanocrystal system. It is also surmised that elemental S likely exists in a vapor phase in large part during milling, considering its low melting point (115 ℃). At 2h 40 min, the Zn peaks decrease further together with the shoulder peaks at 29.1°, with both finally disappearing in 3 h. Thus, the cross-section R3 in Fig. 1(d) includes Cu_2SnS_3, Zn (ZnS), and elemental S based on the aforementioned hypothesis. The detailed reaction pathway can be elaborately confirmed by means of Raman spectroscopy using a laser source with a shorter wavelength.

The abrupt changes in the XRD patterns in Fig. 1(a,b) were consistently observed in the morphological evolution of milled powders investigated using scanning electron microscopy (SEM) as shown in Fig. 2. The elemental powders were agglomerated at tens of micrometers in size and were partly fragmented up to 2 h (Fig. 2(a–c)). Then, sub-micron particles suddenly appeared at 3 h, leaving no trace of the micron-sized particles (Fig. 2(d)). Further milling narrowed the size distribution without a pronounced reduction of the primary particles size (Fig. 2(e,f)). Ductile elements of Zn, Sn, and S are regarded to make large agglomerates in 30 min. The sudden decrease in the particle size at 3 h can be attributed to the formation of a brittle CZTS compound with the complete consumption of the ductile elements in the milled powder.
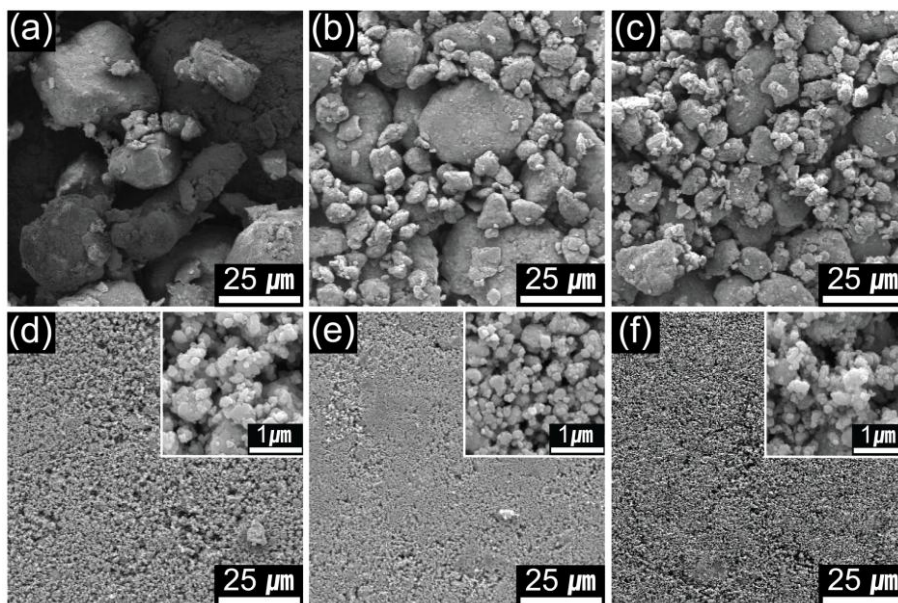
Fig. 2. SEM images of the mixture of Cu, Zn, Sn, and S precursors, ball-milled at 500 rpm for various periods: (a) 30 min, (b) 1 h, (c) 2 h, (d) 3 h, (e) 4 h, and (f) 5 h.

The transmission electron microscopy (TEM) analysis results shown in Fig. 3 reveal the detailed morphology of the as-synthesized nanocrystals prepared after 5 h of ball milling. As shown in Fig. 3(a), fine particles several tens of nanometers in diameter were observed along with their agglomerates of *ca.* one hundred nanometers. The lower bound of the primary particle size of the powder milled for 5 h was estimated by using the XRD peaks according to the Scherrer equation; it was found to be *ca.* 15 nm, which is in fairly good agreement with the TEM results. The high-resolution TEM image shown in Fig. 3(b) indicates that the nanoparticles are crystalline in nature and have lattice fringes with interplanar distances of 0.31, 0.27, and 0.16 nm, which belong to the (112), (200), and (312) planes of kesterite CZTS, respectively. The electron diffraction pattern for the selected area (SAED) marked by the dashed square in Fig. 3(a) is also in agreement with the XRD analysis, comprising a series of diffraction rings with *d*-spacings of 0.31, 0.19, and 0.16 nm that correspond to the (112), (220), and (312) planes of kesterite CZTS. A scanning transmission electron microscopy-energy dispersive X-ray spectroscopy (STEM-EDS) elemental mapping analysis confirms the

compositional homogeneity of all constituent elements inside the particles, as shown in Fig. 3(d).
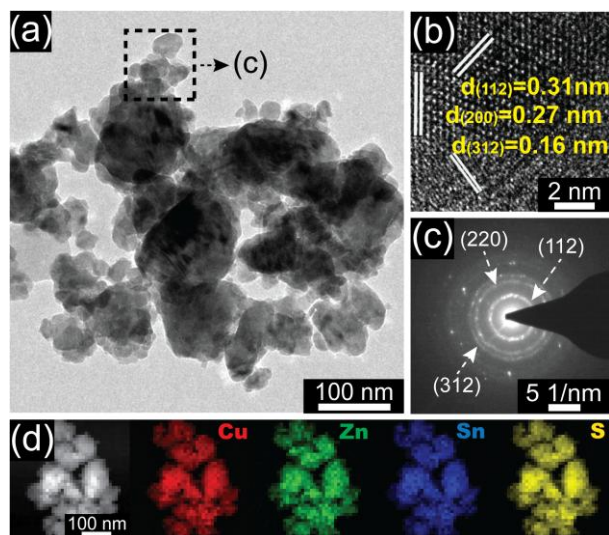
Fig. 3. (a) TEM image with low magnification, (b) high-resolution TEM images, (c) SAED patterns, and (d) STEM-EDS elemental mapping results for the as-synthesized CZTS nanoparticles.

Wada and Hinoshita[26] reported that the mechanochemical synthesis of CuInSe$_2$ proceeds *via* mechanically induced self-propagating reactions during which self-ignition begins after a certain period of activation. Among the distinct characteristics of these self-propagating reactions are a sudden release of heat and the abrupt formation of products.[26,27] The latter is in good accord with the present observations, *i.e.*, the sudden phase transformation into CZTS between 2 h 20 and 2 h 30 min along with the rapid completion of this process in half an hour. Thus, it is suggested that the synthesis of CZTS powder by ball milling also undergoes a mechanically induced self-propagating reaction, as schematically illustrated in Fig. 4. Once the mechanical energy initiates the formation of kesterite CZTS, the heat release corresponding to the formation enthalpy[28,29] of $-405 \sim -337$ kJ mol^{-1} is regarded to accelerate the reaction.
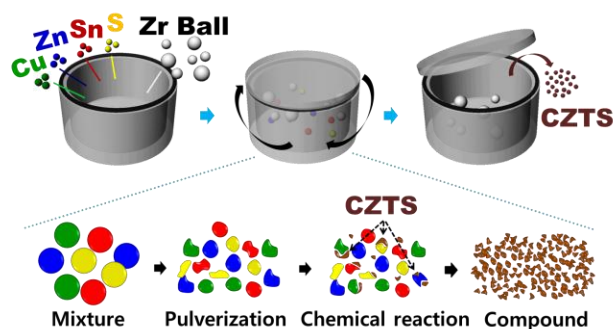
Fig. 4. A schematic illustration of the synthetic procedure of CZTS nanocrystals by a meachnochemical process.

In comparison with previous reports on the synthesis of CZTS by ball milling, the most salient feature of the present results is that CZTS nanocrystals were prepared with a higher degree of phase purity within a much shorter time. Gao *et al*. reported the synthesis of CZTS from the elemental powders by means of planetary ball milling.[18] However, phase-pure CZTS powders were synthesized only with an additional heat treatment at 550 ℃ for 5 h. Our observations agree with that of Gao *et al*. in that the CIGS phase was successfully synthesized in less than 1 h at a milling speed of 200 rpm,[30] whereas CZTS was not created under the same conditions. The above-mentioned enthalpy of formation for CZTS is much lower than that for CuInSe$_2$ (CISe), $-205 \sim -179$ kJ mol^{-1},[31,32] indicating that the formation of CZTS from its elemental components is thermodynamically more favorable than CISe. Therefore, it can be speculated that the CZTS phase requires higher kinetic activation to be formed as compared to CISe. Thus far, only Wang and Gong have succeeded in synthesizing a CZTS phase by solvent-free ball milling alone. It took more than 25 h, however, to obtain the CZTS phase at a decent level of purity with a milling speed of 600 rpm.[17] For comparison, it should be noted that the CZTS nanoparticles in this work were synthesized at a relatively high purity level by a reaction of 3 h at 500 rpm. We attribute this to the optimized

processing variables, in this case the shape of the milling vessel, the material of the grinding balls and their size distribution, the ball-to-powder weight ratio, and the charging volume of a container. A mechanical milling process, especially when using high energy, is subject to contamination from the balls and the jar lining.[16] Therefore, a short milling time and/or milder milling conditions are generally recommended to keep the impurity pick-up during milling as low as possible.

Finally, we would like to emphasize the stability of the present materials. The X-ray photoelectron spectroscopy (XPS) analysis (see Fig. S1† in the Electronic supplementary information (ESI)) shows that the as-synthesized CZTS nanoparticles are free from any oxidized species such as sulfates, which were often observed in previous reports.[16,17] This can also be attributed in part to the shorter reaction time of the present process. Along with this feature, an additional distinctive characteristic of our product is its long-term stability. The CZTSe powder stored on a bench top for one year was found to preserve its phase and compositional purity (Fig. S2† in ESI), implying that it can serve as a bench top chemical.

Characterization of CZTS and CZTSe thin films

Fig. 5 shows the XRD patterns (a) and Raman spectra (b) of the as-deposited CZTS film and a film selenized at 560 ℃ for 10 min under a Se-containing atmosphere. The XRD peak position of the as-coated film was identical to that of the as-synthesized nanoparticles (Fig. 1(a)) aside from Mo (110) reflection originating from the substrate and the slightly reduced intensities after the wet-milling process. Raman scattering peaks for the as-coated film in Fig. 5(b) show a small degree of red shift as compared to those for the as-synthesized powder (Fig. 1(c)); this can be attributed to the strain effect on the rigid substrate. Upon selenization, each XRD peak for the as-coated CZTS was shifted toward the low-angle side due to the lattice expansion associated with Se substitution. At the same time, the peaks were markedly

11

intensified, having much smaller widths compared to the CZTS film, indicating a significant increase in the degree of crystallinity along with grain growth during selenization, which is coincident with the microstructural changes of the films as shown in Fig. 6(a,b). All of the diffraction peaks for the as-sintered film were found to belong to CZTSe (JCPDS card no. 10-6295), as labeled in Fig. 5(a), including very tiny peaks such as the (101) and (110) planes. The Raman spectrum of the as-sintered film in Fig. 5(b) shows two intense peaks at 197 and 173 cm^{-1}, which are in agreement with the A_1 vibration mode for a pure selenide kesterite phase, CZTSe.[20,33] The other peaks, with much lower intensities at 232 and 246 cm^{-1}, can also be assigned to CZTSe.[33,34] Although secondary phases such as $Cu_{2-x}Se$ (260 cm^{-1}),[35] ZnSe (205, 251 cm^{-1}),[36] Cu_2SnSe_3 (180, 236, 251 cm^{-1}),[20] and $MoSe_2$ (168, 240, 285, 350 cm^{-1})[34] were not identified, the existence of ZnSe, in particular, is not excluded considering only this result because the green excitation (*e.g.*, 514.5 nm) is not sensitive enough to detect the small amount of the ZnSe impurity phase.[37] The segregation of ZnSe is often accompanied with the accumulation of Zn element in the concentration depth profiles.[38,39] In this regard, it should be pointed out that the Zn atoms in the present CZTSe films are quite homogeneously distributed throughout the entire thickness, as shown in the depth profile (Fig. 6(d)) measured by Auger electron spectroscopy (AES).
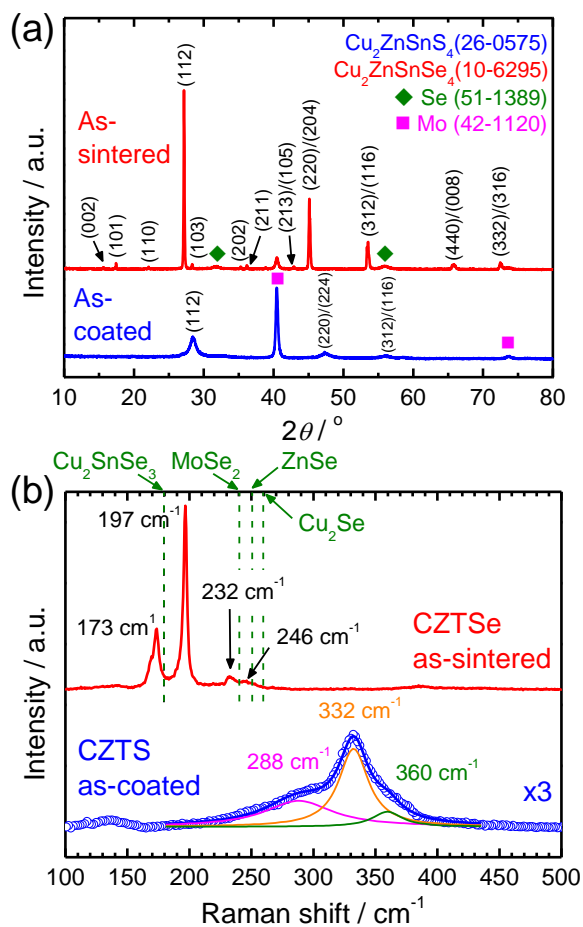
Fig. 5. (a) XRD patterns and (b) Raman spectra (using 514.5 nm excitation) of as-coated CZTS and as-sintered CZTSe films.

Fig. 6(a,b) compares the microstructures of the as-coated and as-sintered films from cross-sectional images. The reactive annealing of the as-coated CZTS nanocrystal film induced substantial grain growth up to *ca.* 1 μm along with the concomitant shrinkage of the film thickness. The cross-section of the as-selenized film demonstrates a uniform microstructure throughout its thickness without a mesoporous bottom layer that is commonly observed during the selenization of CZTS nanocrystal films.[10–12] The compositions of the thin films before and after selenization as determined by EDS are listed in Table 1. The atomic ratios, [Cu] / ([Zn] + [Sn]) and [Zn] / [Sn], of the as-deposited film were found to be 0.76 and

13

1.14, respectively, which are quite close to the initial batch compositions of 0.77 and 1.20, thus supporting the assumption that there was no significant elemental loss during the ball milling process in a closed vessel. Most of the S atoms in the as-deposited film were replaced with Se in the selenized film, which can also be confirmed with the depth profile measurement of the atomic concentration as shown in Fig. 6(c,d). Therefore, the as-sintered film can be nominally designated as CZTSe. The AES depth profiles exhibited a homogeneous distribution of all constituent elements across the thickness of the CZTSe film as its uniform microstructure.
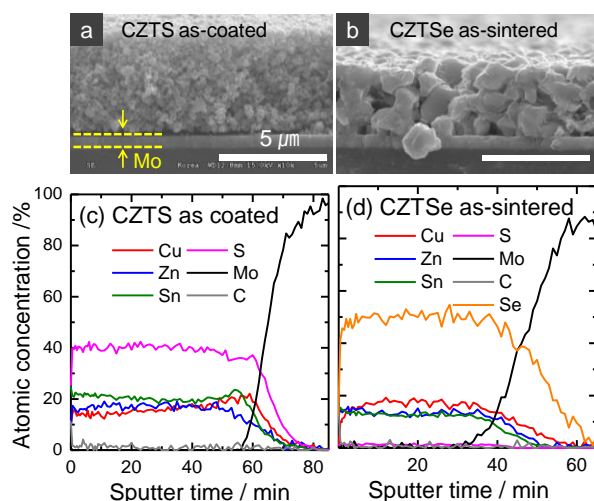
Fig. 6. Typical SEM cross-sections (a,b) and atomic concentration depth profiles measured by AES (c,d) for the as-coated CZTS (left) and as-sintered CZTSe (right) films.

Table 1. Compositions of the as-coated and as-sintered films determined by EDS.

Sample	[Cu] / ([Zn] + [Sn])	[Zn] / [Sn]	[Se] / [cations]	[S] / [cations]
As-coated	0.76 ± 0.01	1.14 ± 0.05	-	1.09 ± 0.06
As-sintered	0.74 ± 0.02	1.29 ± 0.07	0.88 ± 0.06	0.05 ± 0.03

Photovoltaic properties of CZTSe thin films

Solar cell devices with the as-sintered CZTSe film on Mo-coated soda-lime glass substrates were prepared using conventional processes for a chemically deposited CdS buffer layer and sputtered ZnO window layers. Fig. 7 shows the current density–voltage (j–V) characteristics under AM 1.5G illumination (100 mW cm^{-2}) and in the dark, as well as the external quantum efficiency (EQE; η_Q) without a bias light for the resulting device. The best device with the CZTSe film exhibited a power conversion efficiency (η) of 6.11% based on the active area (0.44 cm^2), with a short-circuit current density (j_{SC}) of 31.6 mA/cm^2, an open-circuit voltage (V_{OC}) of 0.423 V, and a fill factor (FF) of 0.457. The bandgap energy (E_g) was estimated from the EQE curve near the band-edge regime as shown in Fig. 7(b). Linear regression on the plot of $[h\nu \cdot \ln(1 - \eta_Q)]^2$ $vs.$ $h\nu$ yielded an E_g value of 1.00 ± 0.03 eV, which is in a good agreement with the theoretically calculated value (1.0 eV)[40] as well as that determined from the absorption measurement (1.02 eV)[38] for the low-bandgap CZTSe. It is worth mentioning that the deficiency in V_{OC} with respect to E_g (*i.e.*, $E_g/e - V_{OC}$) of the present device was found to be 0.577 V, which is comparable to 0.583 V for the best coevaporation-based device ($\eta = 9.15\%$ with $E_g = 0.96$ eV, $j_{SC} = 37.4$ mA/cm^2, $V_{OC} = 0.377$ V, and $FF = 0.649$)[7] and better than the value 0.617 V for the high-efficiency, low-bandgap CZTSe device fabricated using a hydrazine solution method ($\eta = 10.1\%$ with $E_g = 1.04$ eV, $j_{SC} = 38.7$ mA/cm^2, $V_{OC} = 0.423$ V, and $FF = 0.619$).[41] Considering that this "V_{OC}-deficit" is regarded as one of the key factors determining the device performance,[41] the present result suggests the promise of further improvements in the efficiency.
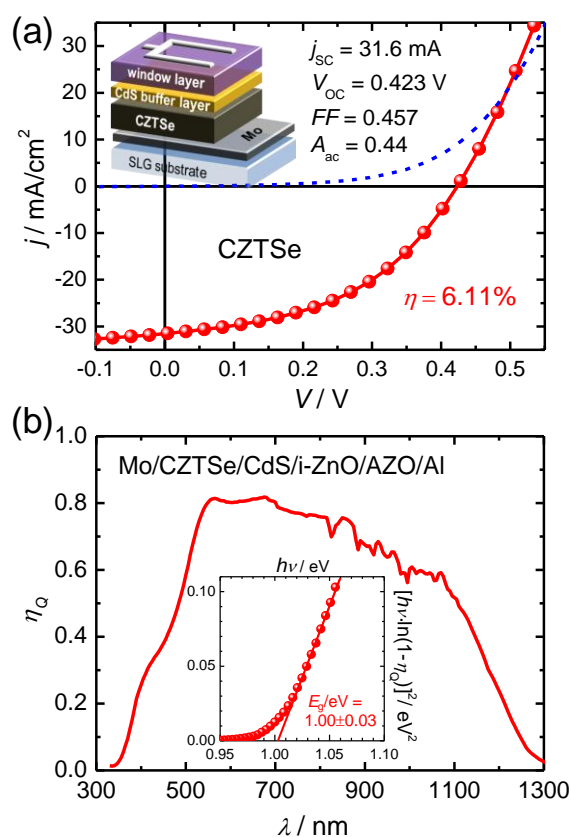
Fig. 7. Photovoltaic performance of the CZTSe thin film solar cell: (a) $j-V$ curves under AM 1.5G illumination and in the dark and (b) EQE (η_Q) without a bias light under short-circuit condition. Inset in part b: $[hv\cdot\ln(1 - \eta_Q)]^2$ *vs. hv* curves near the band-edge regime for estimating the bandgap energy of the absorber films. Note that both the light $j-V$ curve and the EQE were measured without anti-reflection coating.

One of the obvious limiting factors at present is the j_{SC} value (31.6 mA/cm^2), which is still lower than those of the aforementioned devices (37.4 and 38.7 mA/cm^2).[7,41] The EQE spectrum in Fig. 7(b), integrating to 30.4 mA/cm^2 (96% of j_{SC}), exhibited a value of only 0.81 at around 560 nm, which leaves room for improvement when compared to the value of *ca.* 0.95 for the 10.1% device.[41] In addition, the relatively low EQE in the range of 400 to 516 nm indicates that the thickness of the buffer layer should be optimized. The fill factor of the present cell ($FF = 0.46$) is also much lower than those referred to previously. To elucidate the origin of this limited performance, the dark $j-V$ curve was analyzed and the diode parameters

were extracted using the Sites' method.[42] The detailed procedure used to evaluate the parameters is shown in Fig. S3†. The series resistance of the present cell ($R_s = 1.2$ Ωcm^2) was comparable to that of the 10.1% cell.[41] However, the ideality factor ($n = 2.7$) and the reverse saturation current density ($j_0 = 2.4 \times 10^{-2}$ mA/cm^2) was found to be in need of improvement. In particular, the shunt conductance ($G_{sh} = 0.87$ mS/cm^2) was almost three times higher than that of the low-bandgap CuInSe$_2$ device with 8.33% efficiency.[43] It is thus suggested that this high G_{sh} together with the high n resulted in the low FF. The TEM cross-sectional image of the as-prepared device (Fig. S4†) reveals that the high G_{sh} can be unequivocally attributed to the penetrated CdS layer along the open channel of the pores in the absorber layer. Further studies are accordingly in progress to enhance the densification of the absorber layer. It should be noted, however, that the present result exceeding 6% efficiency was achieved with no additional treatments of the absorber layer, such as mechanical pressing,[43] intentional Na-incorporation,[12,44] chemical etching with KCN or HCl solutions,[44,45] or annealing in a Sn-containing atmosphere.[46]
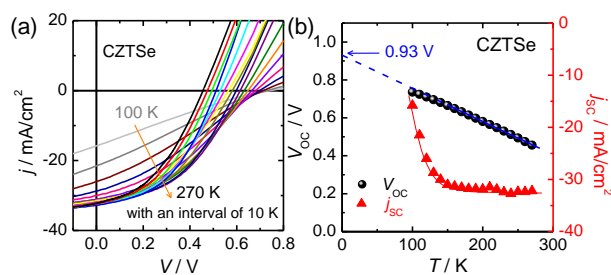
Fig. 8. PV properties of the CZTSe solar cell as a function of T in the range of 100–270 K under 1-sun-equivalent illumination: (a) j–V characteristics and (b) V_{OC} and j_{SC} *vs.* T. Note that the solid line in part b is for visual guidance.

Fig. 8(a) shows the temperature (T) dependence of the j–V characteristics of a CZTSe device under 1-sun-equivalent illumination. The corresponding V_{OC} and j_{SC} as a function of T

are also depicted in Fig. 8(b). As shown in Fig. 8(b), the room temperature j_{SC} remains almost unchanged down to 150 K and then drops abruptly with a further decrease of T. The decrease of j_{SC} at low T was accompanied by the increase of R_s, indicating that thermally-activated processes are working in this T range. In general, these processes could be related to either the carrier free-out effect or the barrier effects against electronic carrier transport, *e.g.*, at the absorber/buffer junction or the Mo/absorber interface.[41] On the other hand, the V_{OC} *vs.* T plot in Fig. 8(b) enables us to extract the activation energy of the predominant recombination process (E_a) corresponding to the *y*-intercept (at $T = 0$) of the linear extrapolation from the high-T regime.[47] The result that we obtained, $E_a = 0.93 \pm 0.01$ V, was slightly lower than E_g (1.00 eV) as determined from the EQE. This implies that the interface recombination process contributes to a certain degree to the total recombination current. Nevertheless, it is noted that the present value for the discrepancy ($E_g - E_a = 0.07$ V) is relatively small as compared to the high-efficiency CZTSe device,[41] which is consistent with the relatively small value for $E_g/e - V_{OC}$ of the present device.

Conclusions

We have demonstrated a simple and environmentally friendly route for fabricating CZTSe solar cells which exhibit promising efficiencies exceeding 6%. An emphasis is placed on the process through which the CZTS nanoparticles are synthesized from readily available elemental precursors without requiring any toxic or expensive solvents. Moreover, the present mechanochemical synthesis provided CZTS nanoparticles on a relatively large scale, which remained air-stable for more than one year. The analysis of the precursor powders at the intermediate stages of milling showed that the CZTS compound was suddenly formed between 2 h 30 min and 3 h, most likely *via* a mechanically induced self-propagating reaction. The doctor-blade coating of CZTS nanoparticles dispersed in an environmentally benign

solvent (ethanol) and subsequent annealing in a Se-containing atmosphere yielded highly

crystalline CZTSe thin films with a grain size of ~1 μm. The resulting CZTSe solar cell

exhibited a better V_{OC}-deficit value (0.58 V) than a state-of-the-art ($\eta = 10.1\%$) CZTSSe

device with a comparable bandgap energy value (1.04 eV). The difference between the V_{OC}

and the activation energy of the recombination current (E_a) was also found to be less than 0.1

eV. Both results demonstrate that the present method is promising when seeking to achieve

highly efficient CZTSe devices. The analysis of the diode parameters together with the TEM

investigation suggests that further improvements in the device performance require the

realization of a better microstructure of the CZTSe film, among other improvements. To this

end, the effects of the film compositions including the cation nonmolecularity, the ratio of S

to Se, and the alkali-ion concentration, which can be easily tailored by adjusting the initial

compositions of the precursors, are under investigation.

Experimental

Synthesis of CZTS nanoparticles

CZTS nanoparticles were synthesized *via* a mechanochemical process using a planetary ball-

mill machine (Fritsch GmBH, pulverisette 5 classic line). Elemental powders of copper (Alfa

Aesar, 99.9%, ~100 mesh), zinc (Alfa Aesar, 99.9%, ~100 mesh), tin (Sigma Aldrich, 99.9%,

~100 mesh), and sulfur (Sigma Aldrich, 99.99%) were weighed as received in a

predetermined molar ratio of Cu : Zn : Sn : S = 1.7 : 1.2 : 1.0 : 4.0. The powder mixture (~20

g in total) was charged into a round-ended stainless steel jar (80 mL in volume) filled with

nitrogen together with zirconia balls (25 g of 5-mm-diameter and 25g of 10-mm-diameter

balls). The ball-to-powder weight ratio (charge ratio) was kept at 5:1. Planetary ball-milling

was carried out under a solvent-free condition at a speed of 500 rpm for a period of 30 min to

5 h. The milled powder samples were intermittently picked up and their phase and

morphological evolution was investigated as a function of the milling time.

Fabrication of CZTSe thin films and solar cells

A colloidal solution (ink, 160 mg/mL) was prepared for non-vacuum film formation by dispersing the as-synthesized CZTS nanoparticles into ethanol followed by mild wet-milling for 12 h using 1- and 5-mm-diameter zirconia balls at a ratio of 7:3. The as-prepared colloidal solution was cast into CZTS precursor films by a doctor-blade method onto Mo-sputtered soda-lime glass substrates ($30 \times 40 \times 1$ mm^3). Sintering was carried out in a Se-containing atmosphere at atmospheric pressure to obtain low-bandgap CZTSe. The precursor films were initially pre-annealed at 300 °C for 30 min and subsequently sintered at 560 °C for 10 min. During the sintering step, a couple of selenium pellets (99.99%, Aldrich) were placed 9 cm away from the thin film at the center of a tube furnace so as to hold the temperature of the selenium to approximately 370 °C, yielding a selenium partial pressure of 2.8×10^{-3} atm.[19] The as-prepared CZTSe thin films were integrated into solar cells in the conventional configuration of Mo/CZTSe/CdS/ZnO/ZnO:Al/Ni/Al. A CdS buffer layer (*ca.* 70 nm in thickness) was deposited onto the CZTSe film *via* chemical bath deposition. The ZnO (50 nm) and ZnO:Al (600 nm) layers were deposited onto the CdS layer using radio-frequency magnetron sputtering. A Ni/Al grid (50 nm / 500 nm) was deposited by thermal evaporation onto the ZnO:Al layer with the remainder of the surface serving as an active area measuring *ca.* 0.44 cm^2. The detailed cell preparation condition is given elsewhere.[19]

Characterizations of materials and devices

The morphologies of nanoparticles and thin films were analyzed by scanning electron microscopy (SEM; FEI Inspect F50) with an acceleration voltage of 5 to 10 kV. The detailed morphologies and compositional distributions of the nanoparticles were investigated by high-

resolution transmission electron microscopy (HRTEM; FEI Titan 80-300) equipped with scanning transmission electron microscopy-energy dispersive X-ray spectroscopy (STEM-EDS). The compositions of the as-coated CZTS and as-sintered CZTSe films were determined by EDS (EDAX PV97-61850-ME). The crystal structure and phase purity were examined by X-ray diffraction (XRD; Bruker D8 Advance) with Cu Kα radiation (λ = 1.5406 Å) and Raman spectroscopy (Horiba Jobin-Yvon LabRam Aramis spectrometer) equipped with an Ar-ion laser excitation source (λ = 514.5 nm). The relative atomic concentration profiles of the thin films were analyzed by Auger electron spectroscopy (AES; Scanning Auger Nanoprobe PHI-700 & LCTOFMS). The current density−voltage (j−V) curves of the solar cells were measured with a class-AAA solar simulator (Yamashita Denso, YSS-50S) after adjusting the light intensity to AM 1.5G 1-sun (100 mW cm^{-2}) using an NREL-calibrated Si solar cell. The current−voltage−temperature (j−V−T) characteristics were analyzed using a cryostat (Linkam Scientific Instruments, LTS420E) from 100 to 270 K with an interval of 10 K under 1-sun-equivalent solar illumination. External quantum efficiencies (EQEs) were investigated with an incident photon-to-current conversion efficiency measurement system (PV Measurements, Inc.) after calibration with NIST-calibrated Si- and Ge-photodiodes in the ranges of 300 to 1000 nm and 900 to 1400 nm, respectively.

Notes and references

[a] *Center for Materials Architecturing, Korea Institute of Science and Technology (KIST), Seoul 136-791, Korea. E-mail: sohyec@kist.re.kr*

^{b} *Department of materials Science and Engineering, Korea University, Seoul 136-701, Korea*

^{c} *Photo-electronic Hybrids Research Center, Korea Institute of Science and Technology (KIST), Seoul 136-791, Korea, E-mail: dklee@kist.re.kr*

^{d} *Department of Nanomaterials Science and Engineering, Korea University of Science and Technology, Daejeon 305-350, Korea*

† Electronic supplementary information (ESI) available: XPS spectra of the as-synthesized CZTS NCs, XRD, Raman, and XPS spectra of the CZTSe NCs right after the synthesis and after being stored for one year, the detailed procedure used to evaluate the device parameters, and TEM cross sections of the CZTSe solar cell. See DOI: 10.1039/b000000x/

‡ These authors equally contributed to this work.

1   K. Ito and T. Nakazawa, *Jpn. J. Appl. Phys.*, 1988, **27**, 2094−2097.

2   H. Katagiri, N. Sasaguchi, S. Hando, S. Hoshino, J. Ohashi and T. Yokota, *Sol. Energy Mater. Sol. Cells*, 1997, **49**, 407−414.

3   Y. X. Zhao and C. Burda, *Energy Environ. Sci.*, 2012, **5**, 5564−5576.

4   K. Ramasamy, M. A. Malik and P. O'Brien, *Chem. Commun.,* 2012, **48**, 5703−5714.

5   W. Wang, M. T. Winkler, O. Gunawan, T. Gokmen, T. K. Todorov, Y. Zhu and D. B. Mitzi, *Adv. Mater.*, 2014, 4, 1301465-1−1301465-5.

6   T. K. Todorov, O. Gunawan, T. Gokmen and D. B. Mitzi, *Prog. Photovoltaics*, 2013, **21**, 82−87.

7.   I. Repins, C. Beall, N. Vora, C. DeHart, D. Kuciauskas, P. Dippo, B. To, J. Mann, W.-C. Hsu, A. Goodrich and R. Noufi, *Sol. Energy Mater. Sol. Cells,* 2012, **101**, 154−159.

8   S. C. Riha, B. A. Parkinson and A. L. Prieto, *J. Am. Chem. Soc.*, 2009, **131**, 12054−12055.

9   C. Steinhagen, M. G. Panthani, V. Akhavan, B. Goodfellow, B. Koo and B. A. Korgel, *J. Am. Chem. Soc.*, 2009, **131**, 12554−12555.

10   Q. Guo, G. M. Ford, W.-C. Yang, B. C. Walker,. E. A. Stach, H. W. Hillhouse and R. Agrawal, *J. Am. Chem. Soc.*, 2010, **132**, 17384−17386.

11   Y. Cao, M. S. Denny, Jr., J. V. Caspar, W. E. Farneth, Q. Guo, A. S. Ionkin, L. K. Johnson, M. Lu, I. Malajovich, D. Radu, H. D. Rosenfeld, K. R. Choudhury and W. Wu, *J. Am. Chem. Soc.*, 2012, **134**, 15644−15647.

12   H. Zhou, T.-B. Song, W.-C. Hsu, S. Luo, S. Ye, H.-S. Duan, C.-J. Hsu, W. Yang and Y. Yang, *J. Am. Chem. Soc.*, 2013, **135**, 15998−16001.

Nanoscale Accepted Manuscript

13   F.-J. Fan, L. Wu and S.-H. Yu, *Energy Environ. Sci.,* 2014, **7**, 190−208.

14   K. Woo, Y. Kim, W. Yang, K. Kim, I. Kim, Y. Oh, J. Y. Kim and J. Moon, *Sci. Rep.,* 2013, **3**, 3069-1−3069-7.

15   Q. W. Tian, X. F. Xu, L. B. Han, M. H. Tang, R. J. Zou, Z. G. Chen, M. H. Yu, J. M. Yang and J. Q. Hu, *CrystEngComm*, 2012, **14**, 3847−3850.

16   C. L. Azanza Ricardo, M. S. Su'ait, M. Müller and P. Scardi*, J. Power Sources*, 2013, **230**, 70−75.

17   Y. Wang and H. Gong, *J. Alloys Compd.*, 2011, **509**, 9627− 9630.

18   F. Gao, S. Yamazoe, T, Maeda, K. Nakanishi and T. Wada, *Jpn. J. Appl. Phys.,* 2012, **51**, 10NC29-1−10NC29-5.

19   Y. S. Lim, J. Jeong, J. Y. Kim, M. J. Ko, H. Kim, B.S. Kim, U. Jeong and D.-K. Lee, *J. Phys. Chem. C*, 2013, **117**, 11930−11940.

20   M. Altosaar, J. Raudoja, K. Timmo, M. Danilson, M. Grossberg, J. Krustok and E. Mellikov, *Phys. Status Solidi A*, 2008, **205**, 167−170.

21   P. A. Fernandes, P. M. P. Salomé and A. F. da Cunha, *J. Alloys Compd.*, 2011, **509**, 7600−7606.

22   P. A. Fernandes, P. M. P. Salomé and A. F. da Cunha, *Thin Solid Films*, 2009, **517**, 2519−2523.

23   X. Fontané, L. Calvo-Barrio, V. Izquierdo-Roca, E. Saucedo, A. Pérez-Rodriguez, J. R. Morante, D. M. Berg, P. J. Dale and S. Siebentritt, *Appl. Phys. Lett.*, 2011, 98, 181905-1−181905-3.

24   R. Schurr, A. Hölzing, S. Jost, R. Hock, R. Vob, J. Schulze, A. Kirbs, A. Ennaoui, M. Lux-Steiner, A. Weber, I. Kötschau and H.-W. Schock, *Thin Solid Films*, 2009, **517**, 2465–2468.

25   A. Fairbrother, X. Fontane, V. Izquierdo-Roca, M. Espindola-Rodriguez, S. Lopez-Marino, M. Placidi, L. Calvo-Barrio, A. Perez-Rodriguez and E. Saucedo, *Sol. Energy Mater. Sol. Cells*, 2013, **112**, 97−105.

26   T. Wada and H. Kinoshita, *J. Phys. Chem. Solids,* 2005, **66**, 1987−1989.

27   L. Takacs, *Prog. Mater. Sci.*, 2002, **47**, 355−414.

28   S. Chen, J.-H. Yang, X. G. Gong, A. Walsh and S.-H. Wei, *Phys. Rev. B*, 2010, **81**, 245204-1−245204-10.

29   T. Maeda, S. Nakamura and T. Wada, *Jpn. J. Appl. Phys.,* 2011, **50,** 04DP07-1−04DP07-6.

30 B.-G. Song, J. H. Jung, G.-N. Bae, H.-H. Park, J.-K. Park and S.-H. Cho. *J. Nanosci. Nanotechnol.,* 2013, **13**, 6042−6051.

31 S. Chen, A. Walsh, X.-G. Gong and S.-H. Wei, *Adv. Mater.*, **2013**, 25, 1522−1539.

32 J. B. Mooney and R. H. Lamoreaux, *Sol. Cells*, 1986, 16, 211−220.

33 P. M. P. Salomé, P. A. Fernandes and A. F. da Cunha, *Thin Solid Films*, 2009, **517**, 2531−2534.

34 A. Redinger. K Hönes, X. Fontané, V. Izquierdo-Roca, E. Saucedo, N. Valle, A. Pérez-Rodríguez and S. Siebentritt, *Appl. Phys. Lett.*, 2011, **98**, 101907-1−101907-3.

35 T. Tanaka, T. Sueishi, K. Saito, Q. Guo, M. Nishio, K. M. Yu and W. Walukiewicz, *J. Appl. Phys.*, 2012, 111, 053522-1−053522-4.

36 M. Grossberg, J. Krustok, J. Raudoja, K. Timmo, M. Altosaar and T. Raadik, *Thin Solid Films*, 2011, **519**, 7403−7406.

37 R. Djemour, M. Mousel, A. Redinger, L. Gütay, A. Crossay, D. Colombara, P. J. Dale and S. Siebentritt, *Appl. Phys. Lett.*, 2013, **102**, 222108-1−222108-4.

38 S. Ahn, S. Jung, J. Gwak, A. Cho, K. Shin, K. Yoon, D. Park, H. Cheong and J. H. Yun, *Appl. Phys. Lett.*, 2010, **97**, 021905-1−222108-3.

39 W.-C. Hsu, I. Repins, C. Beall, C. DeHart, G. Teeter, B. To, Y. Yang, R. Noufi, *Sol. Energy Mater. Sol. Cells*, 2013, **113**, 160−164.

40 S. Chen, X. G. Gong, A. Walsh and S.-H. Wei, *Appl. Phys. Lett.*, 2009, 94, 041903-1−041903-3.

41 S. Bag, O. Gunawan, T. Gokmen, Y. Zhu, T. K. Todorov and D. B. Mitzi, *Energy Environ. Sci.*, 2012, **5**, 7060−7065.

42 J. R. Sites and P. H. Mauk, *Sol. Cells*, 1989, **27**, 411−417.

43 Y. S. Lim, H.-S. Kwon, J. Jeong, J. Y. Kim, H Kim, M. J. Ko, U Jeong and D.-K. Lee, *ACS Appl. Mater. Interfaces*, 2014, **6**, 259−267.

44 Z. Su, K. Sun, Z. Han, H. Cui, F. Liu, Y. Lai, J. Li, X. Hao, Y. Liu and M. A. Green, *J. Mater. Chem. A*, 2014, **2**, 500−509.

45 A. Fairbrother, E. Garcia-Hemme, V. Izquierdo-Roca, X. Fontane, F. A. Pulgarin-Agudelo, O. Vigil-Galan, A. Perez-Rodriguez and E. Saucedo, *J. Am. Chem. Soc.*, 2012, **134**, 8018−8021.

46 A. Redinger, D. M. Berg, P. J. Dale and S. Siebentritt, *J. Am. Chem. Soc.*, 2011, **133**, 3320−3323.

47 V. Nadenau, U. Rau, A. Jasenek and H. W. Schock, *J. Appl. Phys.*, 2000, **87**, 584−593.

Nanoscale Accepted Manuscript